applied sciences

MDPI

Article

BIZON–UGV for Airport Pavement Testing: Mechanics and Control

Marcin Chodnicki [1], Mirosław Nowakowski [1], Paweł Pietruszewski [1], Mariusz Wesołowski [2] and Sławomir Stępień [3,*]

[1] Air Force Institute of Technology, Ksiecia Boleslawa St. 6, 01-494 Warsaw, Poland; marcin.chodnicki@itwl.pl (M.C.); miroslaw.nowakowski@itwl.pl (M.N.); pawel.pietruszewski@itwl.pl (P.P.)
[2] Military Institute of Armoured and Automotive Technology, Okuniewska 1, 05-070 Sulejowek, Poland; mariusz.wesolowski@witpis.eu
[3] Faculty of Control, Robotics and Electrical Engineering, Poznan University of Technology, Piotrowo 3a, 60-965 Poznan, Poland
* Correspondence: slawomir.stepien@put.poznan.pl

Abstract: The paper presents a study of the performance and development of unmanned ground vehicles (UGVs), establishing mathematical and numerical models of the chassis system. The model analysis is performed by 3D software package SolidWorks 2018 with finite element discretization. The mesh modelling and analysis are focused on studying the strength and stiffness of the robotic platform chassis and the distribution of stress and deformation in the extremal condition. The paper also presents an autopilot design with a new cascade control system for the autonomous motion of an unmanned ground vehicle based on proportional–integral–derivative (PID) and feedforward (FF) control. The PID-FF controller is part of a UGV used in a hybrid control system for precise control and stabilization, which is necessary to increase the vehicle motion stability and maneuver precision. The hybrid PID-FF control system proposed for the ground vehicle model gives satisfactory control quality while maintaining the simplicity of the control system. The presented tests performed in mechanical design and control analysis give good results and prove the usefulness of the designed unmanned device.

Keywords: finite element method; mechanical stress and deformation; airport pavement; unmanned ground vehicle; autopilot; proportional–integral–derivative control; feedforward control

Citation: Chodnicki, M.; Nowakowski, M.; Pietruszewski, P.; Wesołowski, M.; Stępień, S. BIZON–UGV for Airport Pavement Testing: Mechanics and Control. *Appl. Sci.* **2024**, *14*, 2472. https://doi.org/10.3390/app14062472

Academic Editor: Dimitris Mourtzis

Received: 7 February 2024
Revised: 27 February 2024
Accepted: 28 February 2024
Published: 15 March 2024

1. Introduction

The use of autonomous robotic systems such as autonomous unmanned ground vehicles (UGVs) in the military world has increased, especially by air and land forces. UGVs integrate modern technology into civil or military units by sensing the environment through remote management or sensor systems and performing basic tasks within the scope of the requirements. Autonomous UGVs, available in different sizes and configurations for various needs, have gained qualities that can fulfill many tasks. Engineers are still planning to target the airport industry as a commercial market for unmanned ground vehicle (UGV) systems. Hence, the area of interest is the airport industry and airport technology (e.g., surface imaging, defect detection, pavement testing, surface assessment, etc.); the incorporation of new, hi-tech platforms is constantly growing in civil and military engineering research [1–3]. The book in [1] only introduces, in a timely fashion, the latest advances and developments in robotics based on their significance and quality, but [2] presents the application of civil autonomous vehicle technology to develop a demonstration of UGVs for the Spanish Army, including the background, architecture, and first field tests. The work in [3] focuses on a unified motion control strategy dedicated to the waypoint following task, realized by a differentially driven robot. The vehicle is assumed to move with limited velocities and accelerations to reduce excessive slip and skid effects. In the context of airport technology, the market related to mobile platforms, especially those dedicated to pavement testing and surface assessment [4,5], is important. Here, the application of the motion planning methods to different pavement inspection tasks, including the illustration of pavement processes, is presented and widely described.

Airport UGVs should continuously ensure a precise assessment of the load-bearing capacity of natural airport surfaces in a continuous way. This specific type of surface occurs at airports and airstrips for private, civil, and military use [6,7]. Routine inspection and maintenance of pavement surfaces are of the utmost importance, especially for runway strips designed for aircraft takeoff and landing at significantly higher speeds.

Natural airport surfaces share one goal: minimizing the negative impacts when an aircraft uses an Airport Functional Element (AFE). Therefore, there is an urgent need to design and implement an autonomous, unmanned measuring device that will continuously determine the load capacity of natural airport surfaces and, thus, increase the safety of flight operations [8]. A thorough review of some of the existing strategies for pothole detection along highways was conducted by [9,10]. There are four types of sensor modalities, vibration-based, vision-based, thermography-based, and LiDAR-based, than can acquire data for pavement inspection. In the case of vibration-based methods, the authors of [11] developed specialized data acquisition hardware mounted on a vehicle to conduct the preliminary evaluation of pavement conditions related to potential cracks along pavement surfaces. Additionally, in [12], researchers developed a Pothole Patrol method for detecting and reporting the surface conditions of runways. In the vision-based area for pothole detection, [13] proposed an unsupervised vision-based method with no additional filtering or training requirements. Moreover, the authors of [14] proposed an algorithm for pothole detection using stereo vision.

The paper proposes a new hi-tech UGV called BIZON as an autonomous measuring platform to determine the load bearing capacity of natural airport runway pavements and pavement layers from unbound mixtures. Figure 1 shows UGV BIZON views.

Figure 1. BIZON—unmanned ground platform view, front view, and rear view.

The platform is the size of a small city car and is dedicated to pavement measurement of natural airport surfaces using a three-wheeled mechanical system. The system consists of one measuring wheel buried in the ground to form a groove of a few centimeters with controlled hydraulic pressure.

The measuring system is rigidly coupled with the BIZON platform chassis; thus, very important from the control and navigation point of view is that the navigation algorithms have been supplemented with software mechanisms to protect from a failure of the measurement system during a planned mission. Briefly, the software elements continuously analyze the measuring wheels' actual position by linear encoders inbuilt to hydraulic actuators and the current cruise deviation generated by the control systems. In specific conditions, the measuring wheels are raised up on command by the mission plan operator, sometimes caused by the vehicle stopping.

The platform is also equipped with a BZYG-unmanned aerial device, which allows the introduction to the geotechnical industry of an innovative method that will be significantly better than currently available methods. The result of the study of the state of the art and analysis of solutions offered by competing entities showed a lack of a product with similar features and functionalities on a global scale.

The state-of-the-art UGV modelling, control, and application analysis provides a broad spectrum of both model-free and model-based approaches [15]. Many propositions, e.g., existing control methods, are still based on typical PID controlled autopilots considering motion limits or control saturation. In this paper and research, using both advantages, we proposed a hybrid method in which the proportional–integral–derivative system with feedforward control, abbreviated as the PID-FF control technique, is used to control the UGV's position and speed. At the same time, the suitably introduced FF component will increase the precision level in tracking the UGV. The novelty and added value of our work is the development of an original autopilot conception based on cascade hybrid PID-FF equipped with a saturation and filtering subsystem, as well as comparative simulation tests for the problem of stabilization of the device's orientation and position.

The paper is organized as follows. Section 2 presents the ground vehicle mechanics model with strain simulations. Section 3 describes the UGV model considering nonholonomic constraints and autopilot design. UGV is used in simulation experiments, and its comprehensive report and analysis can be found in Section 3. Finally, the conclusion is drawn in Section 4.

2. Mechanical Design and Analysis

2.1. Methodology

Numerous software packages are currently available for analyzing and simulating real-world engineering problems, known as Computer-Aided Engineering (CAE).

For example, the SolidWorks 2018 Simulation software module can compute each mechanical system's stress and strain distribution, deformations, and displacements. The module is a good tool for solving mentioned problems through the application of the finite element method (FEM) [16] considering mesh discretization. The FEM uses a numerical technique to find solutions, where a distributed model of the system is described by Partial Differential Equations (PDEs). In other words, FEM is a method for dividing up a highly complex problem into small elements that can be solved in relation to each other. The main features of the FEA method are as follows. The entire solution domain is divided into small finite elements, and over each element, the behavior is described by the displacement of the elements and the material characteristics. All elements are assembled together, and neighboring elements ensure the continuity and equilibrium while providing that the boundary conditions of the actual problem are satisfied; a unique solution can be obtained for the overall system of linear or nonlinear algebra equations with large and sparse matrices [16,17]. The finite element method has recently been employed in mechanical problems other than those of structural analysis, i.e., fluid flow and thermal analysis. It has been improved to permit the solution of nonlinear and linear problems, such as large deformation geometric nonlinearity and/or material property nonlinearity. Finite element methods are extensively used to solve problems that would have been unsolvable only a few years ago [16,17].

The equations in the discrete form of the FEM approach are generated from the Galerkin form [18,19]:

$$\int_{\Omega} (\nabla_s \delta \mathbf{u})^T \mathbf{D} \nabla_s \mathbf{u} d\Omega - \int_{\Omega} (\delta \mathbf{u})^T \mathbf{b} d\Omega - \int_{\Gamma_t} (\delta \mathbf{u})^T \mathbf{t} d\Gamma = 0 \tag{1}$$

where $\mathbf{b}$ is the vector of external body forces, $\mathbf{D}$ is a symmetric positive-definite matrix of material constants, $\mathbf{t}$ is the prescribed traction vector on the natural boundary Γ_t, $\mathbf{u}$ represents trial functions, $\delta\mathbf{u}$ represents test functions, and $\nabla_s \delta \mathbf{u}$ is the symmetric gradient of the displacement field.

The approach uses the following trial and test functions:

$$\mathbf{u}^h(\mathbf{x}) = \sum_{i=1}^{n} \mathbf{N}_i(\mathbf{x}) \mathbf{d}_i \text{ and } \delta \mathbf{u}^h(\mathbf{x}) = \sum_{i=1}^{n} \mathbf{N}_i(\mathbf{x}) \delta \mathbf{d}_i \tag{2}$$

where n is the number of the nodal variables of the element, $\mathbf{d}_i$ is the nodal displacement vector, and $\mathbf{N}_i(\mathbf{x})$ is the shape function matrix.

By substituting the approximations, $\mathbf{u}^h(\mathbf{x})$ and $\delta\mathbf{u}^h(\mathbf{x})$, into the weak form and invoking the arbitrariness of virtual nodal displacements, Equation (1) yields the standard discretized algebraic equation system

$$\mathbf{K}\mathbf{d} = \mathbf{f} \tag{3}$$

where $\mathbf{K}$ is the stiffness matrix; $\mathbf{f}$ is the element force vector that is assembled with entries of

$$\mathbf{K}_{ij} = \int_{\Omega} \mathbf{B}_i^T \mathbf{D} \mathbf{B}_j \mathrm{d}\Omega \tag{4}$$

and

$$\mathbf{f}_i = \int_{\Omega} \mathbf{N}_i(\mathbf{x}) \mathbf{b} \mathrm{d}\Omega + \int_{\Gamma_t} \mathbf{N}_i^T(\mathbf{x}) \mathbf{t} \mathrm{d}\Gamma \tag{5}$$

with the strain gradient matrix

$$\mathbf{B}_i(\mathbf{x}) = \nabla_s \mathbf{N}_i(\mathbf{x}) \tag{6}$$

where operations (4) and (5) are performed for the assumed finite elements considering defined interpolation functions. The functions define and analyze the variation in the displacement matrix within the element and on its surface. To perform continuity, the displacement vector $\mathbf{u}$ must also be continuous over the entire region. This means that the displacements at the common nodes of the internal element boundary of two adjoining elements must be the same. In addition, the functional representations of the displacements over the common boundary must be identical [6,18].

2.2. Numerical Analysis

The main mechanical part of the platform is the chassis. The UGV platform chassis works under vertical forces that simulate the load of two packs of power batteries and hydraulic devices used in the vehicle as a power control system for measuring actuators.

The analysis is performed using models developed in the SolidWorks 2018 software package, computing the stress and deformation considering the mesh based on tetrahedral elements [16]. Figure 2 shows the chassis geometry, where each part is made from steel. Figure 3 shows meshes of the mentioned platform chassis component.

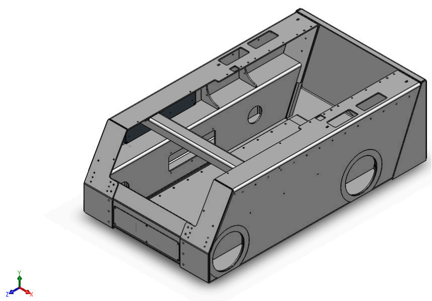

Figure 2. Platform chassis geometry.

For the purpose of the complete analysis, an upper vertical load is considered as a static excitation computing chassis deformation and stress. Simulations are performed for the force acting on the chassis upper elements. The simulations consisted of finding deformations and stress for the force push F = 3000 kg, as shown in Figure 4.

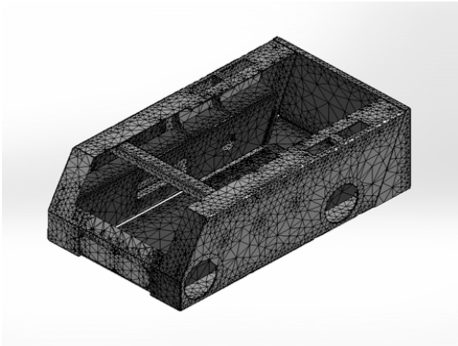

Figure 3. Mesh of the chassis.

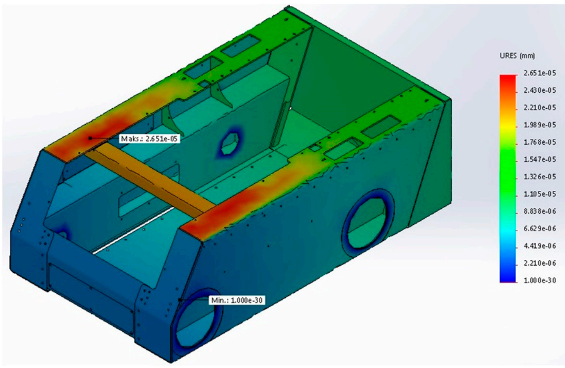

Figure 4. Platform chassis deformation.

The analysis performed for each of the above-mentioned cases shows how working forces excite stress and deformation of the chassis components and indicates areas where the deformation/displacement is dangerous.

Considering static displacement computation for a 3000 kg load (presented in Figure 4), the maximum value of displacement is only $2.65{\cdot}10^{-5}$ mm. It means that the construction strongly satisfies its performance.

Another important element of the mobile platform, a set of actuators with a fixed beam, is examined. The set of actuators creates a platform measuring system for airport pavement testing. The geometry of the subsystem is shown in Figure 5.

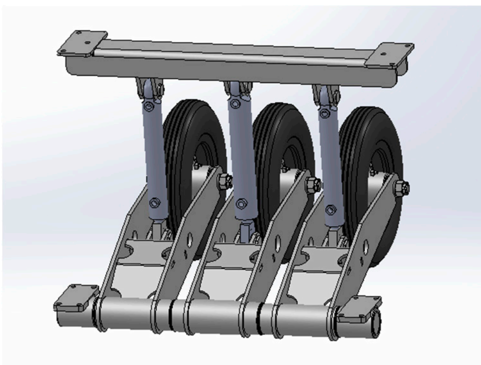

Figure 5. Geometry of the measuring system.

The element is essential from a mechanical point of view because, during the measurement process, the middle hydraulic actuator works under high-pressure conditions. The pressure in the actuator reaches 160 bar, but another actuator also works at about 10% of this value. Figure 6 shows the deformation of applied actuators with mounting beam and fork as a wheel support system.

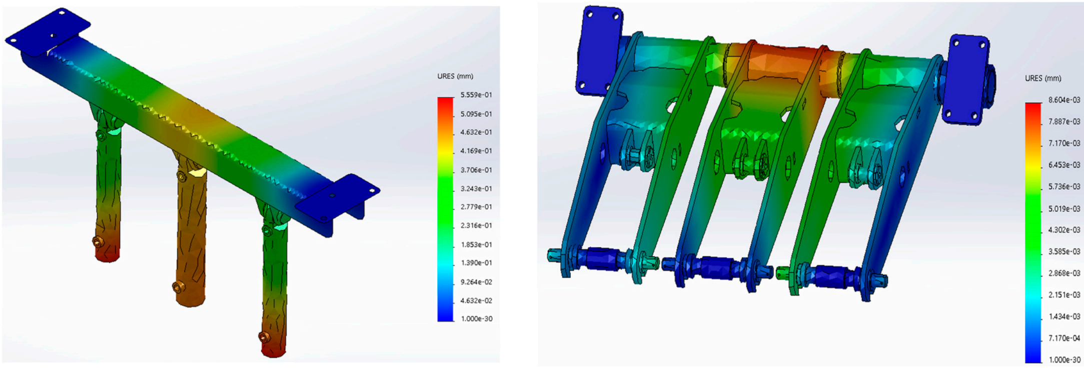

Figure 6. Deformation results, actuator beam, and fork of wheel system.

The result of the simulation using the SolidWorks software package is shown in Figure 6. Consideration of the static displacement computation for extremal forces working on the analyzed beam (left side) shows that the maximum value of displacement is only 0.56 mm. In the case of the fork of the wheeled measuring system (right side), the value of maximum displacement is significantly lower and is only about 0.0086 mm. It means that the construction of the measuring system is well-designed and can be applied in the designed UGV platform.

3. Modelling and Control

Small-tracked vehicle models [20–22] can be approached with differential two-wheeled mobile platforms. A characteristic feature of a two-wheeled vehicle is that it has only two points of contact with the surface. When neglecting slip phenomena of the tracks, perfect contact with the ground is achieved. The transformation from the tracked vehicle model to the wheeled model is commonly obtained by the virtual wheel method [1,5,22]. Tracked mobile platform approximation employing a wheeled platform model with differential drive is simple, more universal, and very useful from a control point of view.

3.1. Mathematical Model

As shown in Figure 7, the model of the Bizon platform can be described considering generalized coordinates $\mathbf{q}(t) = \begin{bmatrix} x_c & y_c & \Theta_r & \Theta_l \end{bmatrix}^T$ in global reference frame XY. The body frame origin lies at the center of mass (CoM), where a pair (x_c, y_c) describes the CoM position, (Θ_r, Θ_l) are angles of the right and left wheels, and ψ is the platform heading angle.

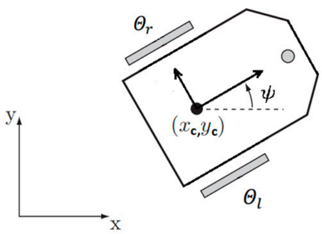

Figure 7. Mobile platform model. Differential wheel approach.

As described in [15], the mobile platform dynamics can be represented by the following motion equation considering friction, Coriolis, and centrifugal forces, but also non-holonomic constraints:

$$\mathbf{M}(\mathbf{q})\ddot{\mathbf{q}} + \mathbf{B}\dot{\mathbf{q}} + \mathbf{C}(\mathbf{q}, \dot{\mathbf{q}}) + \mathbf{A}^T(\mathbf{q})\boldsymbol{\lambda}(t) = \mathbf{E}\boldsymbol{\tau}(t). \tag{7}$$

In Equation (7), $\mathbf{M}(\mathbf{q})$ is a mass and inertia matrix, and $\mathbf{C}(\mathbf{q},\dot{\mathbf{q}})$ is a Coriolis and centrifugal vector:

$$\mathbf{M}(\mathbf{q}) = \begin{bmatrix} m_b + 2m_{wt} & 0 & -\frac{m_{wt}rd}{b}s\psi & \frac{m_{wt}rd}{b}s\psi \\ 0 & m_b + 2m_{wt} & \frac{m_{wt}rd}{b}c\psi & -\frac{m_{wt}rd}{b}c\psi \\ -\frac{m_{wt}rd}{b}s\psi & \frac{m_{wt}rd}{b}c\psi & m_{33} & m_{34} \\ \frac{m_{wt}rd}{b}s\psi & -\frac{m_{wt}rd}{b}c\psi & m_{43} & m_{44} \end{bmatrix},\ \mathbf{C}(\mathbf{q},\dot{\mathbf{q}}) = \begin{bmatrix} -2m_{wt}\dot{\psi}^2 c\psi \\ -2m_{wt}\dot{\psi}^2 s\psi \\ 0 \\ 0 \end{bmatrix},$$

where m_b is the mass of the platform base, m_{wt} is the mass of the wheels with the track, r is the substitute wheel radius, I_{zzb} is the base moment of inertia, I_{yyw} and I_{zzw} are moments related to the wheels, b is the platform width, and d is the distance between the center of mass and wheel axis. Mass coefficients m_{33}, m_{34}, m_{43}, m_{44} are defined as follows:

$m_{33} = r^2\left(2m_w\left[b^2 + d^2\right] + I_{zzb} + 2I_{zzw}\right)/(4b^2) + I_{yyw}$,
$m_{34} = -r^2\left(2m_w\left[b^2 + d^2\right] + I_{zzb} + 2I_{zzw}\right)/(4b^2)$,
$m_{43} = m_{34}$,
$m_{44} = r^2\left(2m_w\left[b^2 + d^2\right] + I_{zzb} + 2I_{zzw}\right)/(4b^2) + I_{yyw}$.

The other matrices in (7) denote the following: $\mathbf{A}(\mathbf{q})$ is a constraint matrix, $\mathbf{B}$ is a friction coefficient matrix, and $\mathbf{E}$ is a matrix related to the wheel torques:

$$\mathbf{A}(\mathbf{q}) = \begin{bmatrix} -s\psi & c\psi & 0 & 0 \\ -c\psi & -s\psi & \frac{r}{2} & \frac{r}{2} \end{bmatrix},\ \mathbf{E} = \begin{bmatrix} 0 & 0 \\ 0 & 0 \\ 1 & 0 \\ 0 & 1 \end{bmatrix},\ \mathbf{B} = \begin{bmatrix} b_{11} & 0 & 0 & 0 \\ 0 & b_{22} & 0 & 0 \\ 0 & 0 & b_{33} & 0 \\ 0 & 0 & 0 & b_{44} \end{bmatrix},$$

where b_{11}, b_{22} are coefficients related to the linear motion and b_{33}, b_{44} are coefficients related to angular speed. Matrix $\mathbf{S}(\mathbf{q})$ is introduced to omit constraints of the mobile vehicle and performs $\mathbf{A}(\mathbf{q})\mathbf{S}(\mathbf{q}) = 0$**.** The $\mathbf{S}(\mathbf{q})$ matrix has the following form:

$$\mathbf{S}(\mathbf{q}) = \begin{bmatrix} \frac{r}{2}c\psi & \frac{r}{2}c\psi \\ \frac{r}{2}s\psi & \frac{r}{2}s\psi \\ 1 & 0 \\ 0 & 1 \end{bmatrix},\ \text{where } s\psi = sin\psi \text{and } c\psi = cos\psi.$$

Multiplying Equation (7) by $\mathbf{S}^T(\mathbf{q})$

$$\mathbf{S}^T(\mathbf{q})\mathbf{M}(\mathbf{q})\ddot{\mathbf{q}} + \mathbf{S}^T(\mathbf{q})\mathbf{B}\dot{\mathbf{q}} + \mathbf{S}^T(\mathbf{q})\mathbf{C}(\mathbf{q},\dot{\mathbf{q}}) = \boldsymbol{\tau}(t) \tag{8}$$

and introducing wheel speed $\mathbf{v} = \begin{bmatrix} \dot{\Theta}_r & \dot{\Theta}_l \end{bmatrix}^{\boldsymbol{T}}$, the platform coordinates' first derivation is

$$\dot{\mathbf{q}} = \mathbf{S}(\mathbf{q})\mathbf{v} \tag{9}$$

and the second derivation is

$$\ddot{\mathbf{q}} = \dot{\mathbf{S}}(\mathbf{q})\mathbf{v} + \mathbf{S}\dot{\mathbf{v}}(\mathbf{q}). \tag{10}$$

Finally, with respect to (9) and (8), a single global state-space affine system of equations describes the platform dynamics:

$$\begin{bmatrix} \dot{\mathbf{q}} \\ \dot{\mathbf{v}} \end{bmatrix} = \begin{bmatrix} \mathbf{S}\mathbf{v} \\ -\left(\mathbf{S}^T\mathbf{M}\mathbf{S}\right)^{-1}\left[\left(\mathbf{S}^T\mathbf{M}\dot{\mathbf{S}} + \mathbf{S}^T\mathbf{B}\mathbf{S}\right)\mathbf{v} + \mathbf{S}^T\mathbf{C}\right] \end{bmatrix} + \begin{bmatrix} 0 \\ \left(\mathbf{S}^T\mathbf{M}\mathbf{S}\right)^{-1} \end{bmatrix}\boldsymbol{\tau}(t) \tag{11}$$

which can also be written as

$$\begin{bmatrix} \dot{\mathbf{q}} \\ \dot{\mathbf{v}} \end{bmatrix} = \begin{bmatrix} \mathbf{S}\mathbf{v} \\ \left(\mathbf{S}^T\mathbf{M}\mathbf{S}\right)^{-1}\left(\boldsymbol{\tau}(t) - (\mathbf{S}^T\mathbf{B}\mathbf{S} + \mathbf{S}^T\mathbf{M}\dot{\mathbf{S}})\mathbf{v} - \mathbf{S}^T\mathbf{C}\right) \end{bmatrix},\ ^{*} \tag{12}$$

where $\boldsymbol{\tau}(t) = \begin{bmatrix} \tau_r & \tau_l \end{bmatrix}^T$ is an input torque vector.

3.2. Control System and Autopilot Design

The autopilot for the UGV Bizon [23,24] is depicted in Figure 8. The main purpose is to follow the reference trajectory or path and speed commands issued in the path planner.

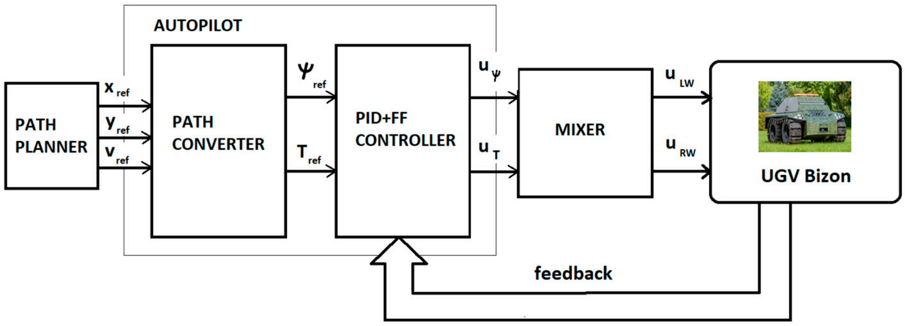

Figure 8. The autopilot design.

The structure consists of a path planner, reference path (reference motion position), speed converter, feedback loop controller of the heading angle ψ rate, and wheel torques based on the PID technique. The autopilot also includes the feedforward component and a reference model that specifies the desired response to a step command. Finally, the turn angle and wheel torque signals are fed to the mixer, which converts it to the right and left wheel torque or speed scaled in the domain of inverter frequency. Hence, the presented block diagram generally represents the implemented control algorithms. Figure 8 shows that the control portion consists of a block named "Path Converter" and "PID+FF Controller". In simplified terms, feedforward control is determined based on set values defined from the current platform position, desired speed, and cross-track error (XTE). The control of the platform's deviation angle is cascaded through the control of angular velocity **r**. This velocity is limited, and these limitations, as well as the XTE error, allow for determining the initial control value. This value is then fine-tuned by an additional PID regulator (Distance To Heading), which determines the course correction based on the distance from the route. Additionally, the BIZON platform is equipped with inverters that maintain the desired wheel rotation frequency regardless of external conditions, which directly affects the speed. Knowing the inverter parameters, gear ratios, and wheel parameters, the set frequency value is determined as feedforward feedback in relation to the desired speed. Subsequently, the external regulator enables real-time speed control in response to the actual speed error determined by a state observer based on GPS receiver data, acceleration sensors, and encoders.

Based on introduced waypoints and current platform position, the autopilot determines trajectory in two modes: with and without tightening (a special function to obtain better mission accuracy, which means tightening to the reference trajectory, minimizing tracking error). When the tightening function is off, only the actual position and reference position are considered in the control process. When the tightening mode is on, the cross-track error (XTE) is considered a function of the distance from the reference trajectory, in this case, the line between two waypoints. The sum of the position error and XTE is considered to determine the motion trajectory and heading angle of the platform. In the case of a very slow platform speed, the motion trajectory computation is problematic and inaccurate.

As shown in Figure 8, one of the simplified modules in the autopilot structure is the PID and FF controller. The PID controller performs UGV control and stabilization in the context of heading angle ψ. It is additionally equipped with the FF component to obtain a quick response due to the reference values. Figure 9 shows the structure of the PID-FF controller and explains its role in the control system.

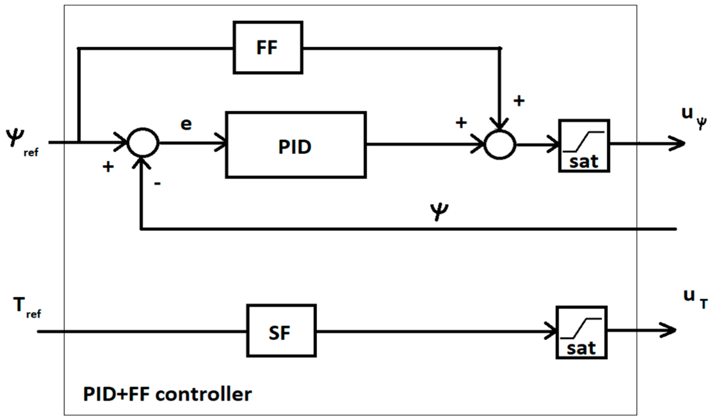

Figure 9. The PID-FF controller.

PID control stands for proportional, integral, and derivative control and is the most commonly used control technique in industry [25,26]. It works in a closed-loop configuration to minimize control error e. Feedforward control (FF) is a strategy used to reject persistent disturbances from ψ_{ref} that cannot adequately be rejected with feedback PID control. Feedforward control is added to feedback control and is not implemented alone. In this situation, the performance of control systems can be greatly enhanced by applying feedforward control. The output of a PID-FF controller is calculated in the time domain from the feedback heading angle and its reference error as follows:

$$u_{\psi} = \mathrm{sat}\left\{k_P e + k_I \int edt + k_D \frac{de}{dt} + k_{FF}\psi_{ref};\ u_{\psi,min}, u_{\psi,max}\right\}, \tag{13}$$

where k_P, k_I, k_D are proportional, integral, derivative gains, and k_{FF} is feedforward gain, as a compromise between reference and process gains.

Feedback control does not provide predictive control action to compensate for the effects of known or measurable disturbances. In that case, feedforward controllers are capable of achieving perfect control if it is physically achievable. However, an approximate model should be available to use feedforward control effectively. In particular, it is important to know how the controlled variable responds to changes in both the disturbance and manipulated variables. Hence, the quality of feedforward control depends on the accuracy of the plant model. Working with a feedback PID controller, with good UGV dynamics modelling or approximation, may be very useful and effective.

The PID-FF controller output must be bounded by the implementing subsystems that introduce saturation, because of the stability problem. In practice, it is obvious that all quantities have upper and lower limits. In addition to improving the disturbance rejection task, a dedicated low-pass filter (LPF) is desirable.

As shown in Figure 9, the wheel torque is only scaled and limited by the saturation subsystem, commonly due to the range of drive converter frequency. Then, merging u_T within the turn control signal u_{ψ} in the mixer, the controller allows the system to output left and right wheel control signals u_{LW} and u_{RW} (Figure 8).

3.3. Experiment and Measurement

To demonstrate the effectiveness and usefulness of the proposed unmanned device in the context of trajectory tracking by autopilot and drives, as well as the designed mechanics, the mobile robotic platform BIZON was tested in real working conditions on the airport board, as shown in Figure 10.

Figure 10. UGV BIZON on the airport board.

The airport is located a few kilometers from Warsaw (the capital of Poland). The average elevation of the airport above sea level is 104 m. The basic element of the airport infrastructure is a runway made of asphalt concrete with concrete thresholds of a total length of 2500 m and a width of 45 m, with geographical directions 261° and 081° where the tests were performed.

To check the correctness of the mechanics and control system of the device, a waypoint trajectory was applied on autopilot and tested considering two cases:

(a) typical PID-FF trajectory control;
(b) the PID-FF with tightening to the trajectory.

For testing purposes, the UGV is equipped with proprietary electronics and software. The only off-the-shelf components are the inverters. The navigation systems of the BIZON platform are based on GNSS RTK working differentially, allowing for the determination of the deviation angle even in static conditions (without movement). The state observer is based on inertial sensors and an extended Kalman filter, where data fusion utilizes information from the GNSS receiver, as well as encoders mounted in the propulsion system. The platform communicates with the command post using encrypted wireless communication. Data acquisition and recording occur both on board and at the command post. BIZON has an extensive telemetry system, and the applied communication with a bandwidth of up to 6 Mb/s allows for the transmission of a large amount of data for real-time and subsequent analysis.

The realized trajectory was compared to a simulation of the vehicle behavior considering models (11)–(12) and control law (13). Table 1 presents the most important BIZON parameters. The included parameters are defined in Section 3, which describes modelling and control technique.

Table 1. BIZON parameters.

Parameter	Value [Quantity]
m_b	2000 [kg]
m_{wt}	200 [kg]
r	0.6 [m]
d	0.5 [m]
I_{zzb}	21.2 [kg.m^2]
I_{zzw}	0.02 [kg.m^2]
I_{yyw}	0.27 [kg.m^2]

Reference trajectory data were inserted into the autopilot as a waypoint. This way, lines that connect via inserted points define a trajectory. For this purpose, using the GNSS RTK module mounted on the robotic platform determined its geographic coordinates, which are presented in Table 2.

Table 2. Trajectory coordinates.

Point nr.	Geographic Coordinates		Distance between Points [m]	Heading Angle [°]
	Latitude	Longitude		
1	52°26′59.461″ N	20°40′25.917″ E	-	63.2
2	52°27′0.2500″ N	20°40′28.467″ E	54.4	151.0
3	52°26′59.449″ N	20°40′29.201″ E	28.6	248.6
4	52°26′58.849″ N	20°40′26.691″ E	51.0	140.7
5	52°26′58.446″ N	20°40′27.240″ E	16.5	

The data can also be stored in the Remote Control Station (RCS) until the radio wireless connection works. The autopilot connecting with the RCS has implemented a special diagnostic algorithm to check the performance of the automatic control mode (full autonomy mode). In critical situations, the algorithm may not be able to work in fully automatic mode, in which case a checklist of failures and inefficient elements is generated.

Before the experiment, the trajectory coordinates were introduced to the platform device via a special software package of RCS 6.8 and visualized using the Google Earth tool. Visualization is presented in Figure 11a,b with numbered waypoints and indicated waypoint distance, where subfigure b to the right shows a zoomed-in view. Red and yellow line show reference trajectory. In addition, the distance between waypoints is indicated above yellow path.

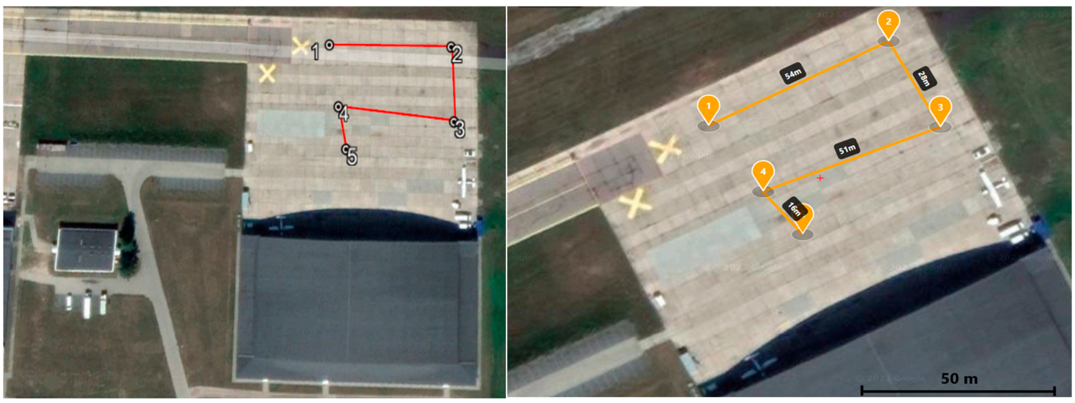

(**a**) (**b**)

Figure 11. Reference waypoint trajectory: (**a**) view with numbered waypoints, (**b**) zoomed-in view.

Firstly, the control system simulations and waypoint trajectory realization were examined. For tests, the device model described in Section 3.1 was considered. The device model started from point no. 1 with assumed zero initial position and zero initial speed: $\mathbf{q}(0) = \begin{bmatrix} 0 & 0 & 0 & 0 \end{bmatrix}^T$ and $\dot{\mathbf{q}}(0) = \begin{bmatrix} 0 & 0 & 0 & 0 \end{bmatrix}^T$. At each waypoint, the initials were zeroing the whole tracking process.

Results of numerical simulations are presented in Figure 12.

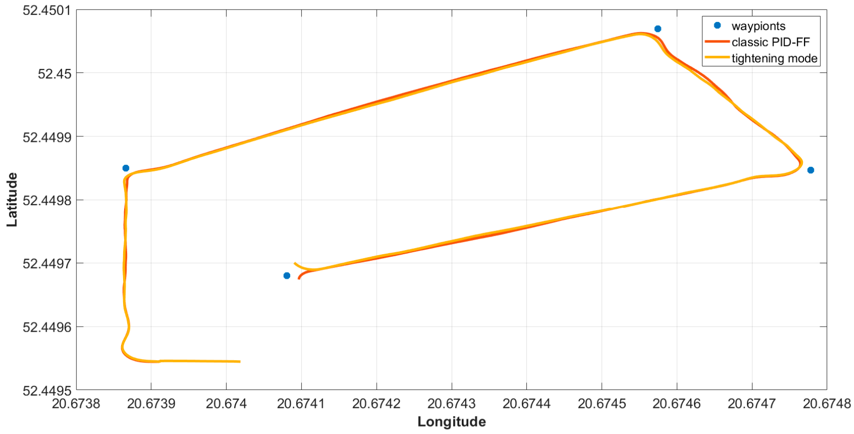

Figure 12. Simulation result of performed trajectory.

The mobile platform realized the defined waypoint trajectory, shown in Figure 11, with the desired cruise speed of 5 km/h. The tightening function was also activated to compare with classic PID-FF control. Figure 13 shows the trajectory performance of the UGV when the tightening function was deactivated. The numbers denote following trajectory waypoints.

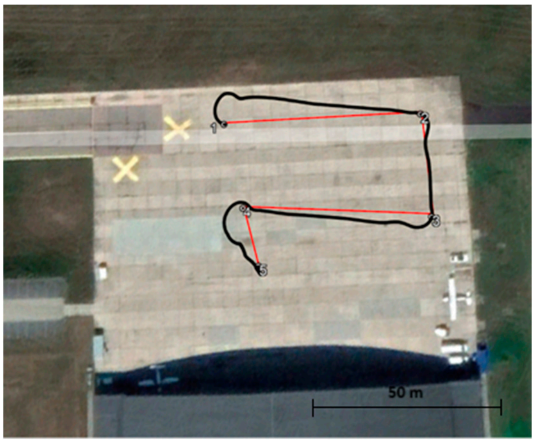

Figure 13. UGV trajectory without tightening (red line—reference path, black line—platform path).

Figure 14 shows the realized waypoint trajectory by UGV with an activated tightening function.

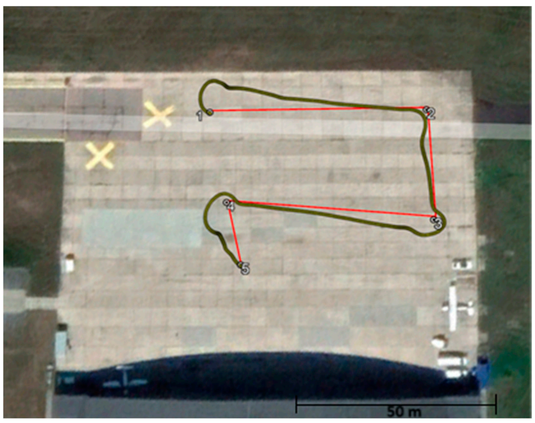

Figure 14. UGV trajectory with tightening (red line—reference path, black green line—platform path).

Realized cases can be compared and shown in one common picture for a better view. Figure 15 presents the two cases: PID-FF and PID-FF with activated tightening function. The difference is clearly visible and similarly as in Figure 13, numbers denote following trajectory waypoints.

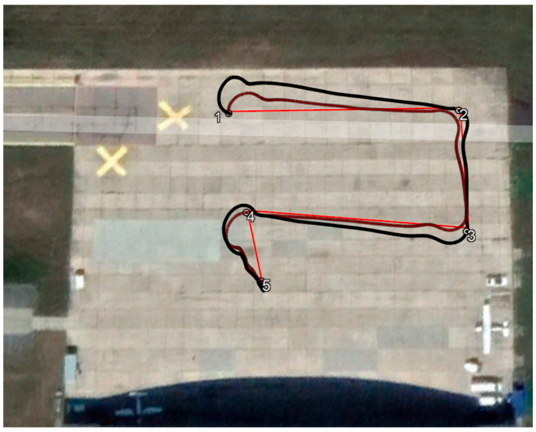

Figure 15. Trajectory comparison (red line—reference path, black line—platform path without tightening, brown line—platform path in tightening mode).

The PID-FF (proportional–integral–derivative with feedforward)-based control algorithm enables the unmanned ground vehicle (UGV) to accurately follow a path delineated by a series of trajectory points, herein referred to as waypoints. This way, the course path consists of line sections that connect indicated waypoints. Hence, based on the current platform position, the platform moves to the destination point (waypoint) with the desired driving course obtained from heading angle computation. This means that as a result, the platform does not realize the course by the line between waypoints, only by being next to or along it. The situation is different when the tightening function is activated. Then, with the actual platform position and orientation, i.e., the distance between the platform and the path line, a course correction is computed and added to the control. This way, the platform can move precisely along the line section determined from the two indicated waypoints.

The performed tests proved the usefulness and effectiveness of the implemented control and navigation algorithms in the autopilot subsystem. Considering RTK correction in the navigation system GNSS RTK/INS, the accuracy of tracking in the context of geographic coordination did not exceed 0.1 m. Still, in the case of relative position, the accuracy was lower than 0.01 m. Neglecting the RTK correction, the autopilot system realized a trajectory with an accuracy of about 0.4 m. Therefore, a measurement system based on GNSS RTK was employed to achieve precision in deviation angle, position, and speed. This sensor is a component of an advanced state observer. In the studies described in the article, the steady-state speed error is up to 0.2 km/h, while the XTE is below 0.5 m.

Additionally, performance of the waypoint trajectory, i.e., platform mission, and the effectiveness and correctness of important software elements were tested in the context of a measurement system failure. When the platform works in tightening mode, a huge value of the heading angle may cause the platform to stop and hide the measurement subsystem. To drop off the subsystem, many conditions must be met. One of them is the value of heading angle error or cruise error, XTE, and finite time criteria related to performing the trajectory.

The control system works perfectly, but it would be good to update it by adding an optimal control functionality that will reduce power consumption from the platform's power supply system. This is a problem that needs to be solved in the future.

4. Conclusions

This paper presents a study of the performance of an unmanned ground robotic device (UGV) that shows the performance of mechanical design. A numerical simulation of the chassis system and pavement measurement subsystem by three-dimensional finite element analysis confirms the strength and stiffness of the vehicle's most crucial mechanical parts. It shows the distribution of stress and deformation under extreme conditions.

The paper also presents an autopilot design based on proportional–integral–derivative (PID) and feedforward (FF) control. The presented tests of the control system show and confirm that precise trajectory control works and gives a satisfactory quality.

The presented tests and measurements prove that the mechanical design and control system works and performs objectively, with respect to precise tracking, speed control, and positioning. Due to the vehicle dynamics, the control method seems promising for analyzing and testing pavement at airports or ground airstrips.

Future work can relate to implementing a new control system based on suboptimal techniques that increase the vehicle's autonomy, which is associated with our concept of the most autonomous UGV BIZON. The implementation of new optimal control techniques is crucial to enhance the autonomy of UGVs. The technique is based on an infinite time control problem. It will be applied to the system of autonomous platforms to measure the load bearing capacity of natural airport runway pavements with a nonlinear feedback compensator. This is a promising and rapidly emerging method of optimal control input that minimizes energy delivered to the mobile platform control system and energy lost when performing mission tasks.

After the new control is implemented, we plan to test the vehicle's behavior at the airport and compare its work to that of the actually implemented PID-FF control.

Author Contributions: Methodology: M.C. and P.P.; hardware and software: M.C. and P.P.; validation: M.W. and S.S.; writing—original draft preparation: S.S.; writing—review and editing: M.W. and S.S.; supervision: M.W., M.N. and S.S. All authors have read and agreed to the published version of the manuscript.

Funding: This research was partially funded by the National Centre for Research and Development in Poland, project no.: POIR.01.01.01-00-0919/19.

Institutional Review Board Statement: Not applicable.

Informed Consent Statement: Not applicable.

Data Availability Statement: The raw data supporting the conclusions of this article will be made available by the authors on request.

Acknowledgments: The authors would like to thank Damian Dobrowolski (Dobrowolski LLC Company) for his support during the design of the mechanical system and the production of the device. We would like also to express our sincere appreciation to Damian for his valuable and constructive talks, suggestions, and comments during the writing and development of this research work.

Conflicts of Interest: The authors declare no conflicts of interest.

References

1. Singh, S. *The DARPA Urban Challenge: Autonomous Vehicles in City Traffic*; Springer: Berlin/Heidelberg, Germany, 2009; Volume 11.
2. Naranjo, J.E.; Clavijo, M.; Jimenez, F.; Gomez, O.; Rivera, J.L.; Anguita, M. Autonomous vehicle for surveillance missions in off-road environment. In Proceedings of the IV IEEE Intelligent Vehicles Symposium, Gothenburg, Sweden, 19–22 June 2016; pp. 98–103.
3. Pazderski, D. Waypoint Following for Differentially Driven Wheeled Robots with Limited Velocity Perturbations. Asymptotic and Practical Stabilization Using Transverse Function Approach. *J. Intell. Robot. Syst.* **2017**, *85*, 1–23. [CrossRef]
4. Tseng, Y.-H.; Kang, S.-C.; Chang, J.-R.; Lee, C.-H. Strategies for autonomous robots to inspect pavement distresses. *Autom. Constr.* **2011**, *20*, 1156–1172. [CrossRef]
5. Chang, J.-R.; Tseng, Y.-H.; Kang, S.-C.; Tseng, C.-H.; Wu, P.-H. The Study in Using an Autonomous Robot for Pavement Inspection. In Proceedings of the 24th International Symposium on Automation and Robotics in Construction, Kochi, India, 19–21 September 2007; pp. 229–234.
6. Nowakowski, M. Perception technology for conversion of off-road vehicles for the purposes of unmanned missions. *J. Civ. Eng. Transp.* **2023**, *5*, 15–27. [CrossRef]
7. Kelner, J.M.; Burzynski, W.; Stecz, W. Modeling UAV swarm flight trajectories using Rapidly-exploring Random Tree algorithm. *J. King Saud. Univ.-Comput. Inf. Sci.* **2024**, *36*, 101909. [CrossRef]

8. Mei, A.; Zampetti, E.; Di Mascio, P.; Fontinovo, G.; Papa, P.; D'Andrea, A. ROADS—Rover for Bituminous Pavement Distress Survey: An Unmanned Ground Vehicle (UGV) Prototype for Pavement Distress Evaluation. *Sensors* **2022**, *22*, 3414. [CrossRef] [PubMed]
9. Coenen, T.B.; Golroo, A. A review on automated pavement distress detection methods. *Cogent Eng.* **2017**, *4*, 1374822. [CrossRef]
10. Kim, T.; Ryu, S.K. Review and analysis of pothole detection methods. *J. Emerg. Trends Comput. Inf. Sci.* **2014**, *5*, 603–608.
11. Yu, B.X.; Yu, X. Vibration-based system for pavement condition evaluation. In *Applications of Advanced Technology in Transportation*; ASCE: Reston, VA, USA, 2006; pp. 183–189.
12. Eriksson, J.; Girod, L.; Hull, B.; Newton, R.; Madden, S.; Balakrishnan, H. The pothole patrol: Using a mobile sensor network for road surface monitoring. In Proceedings of the 6th International Conference on Mobile Systems, Applications, and Services, Breckenridge, CO, USA, 17–20 June 2008; pp. 29–39.
13. Buza EOmanovic, S.; Huseinovic, A. Pothole detection with image processing and spectral clustering. In Proceedings of the 2nd International Conference on Information Technology and Computer Networks, Mathura, India, 9–10 March 2013; Volume 810, p. 4853.
14. Zhang, Z.; Ai, X.; Chan, C.K.; Dahnoun, N. An efficient algorithm for pothole detection using stereo vision. In Proceedings of the 2014 IEEE International Conference on Acoustics, Speech and Signal Processing (ICASSP), Florence, Italy, 4–9 May 2014; pp. 564–568.
15. Korayem, M.H.; Nekoo, S.R.; Korayem, A.H. Finite time SDRE control design for mobile robots with differential wheels. *J. Mech. Sci. Technol.* **2016**, *30*, 4353–4361. [CrossRef]
16. Akin, J. (Ed.) *Finite Element Analysis Concepts via SolidWorks*; World Scientific: Singapore, 2009.
17. Kurowski, P.M. *Engineering Analysis with SW Simulation Professional 2006*; SDC Publishing: Mission, KS, USA, 2006.
18. Dohrmann, C.R.; Key, S.W.; Heinstein, M.W.; Jung, J. A least squares approach for uniform strain triangular and tetrahedral finite elements. *Int. J. Numer. Methods Eng.* **1998**, *42*, 1181–1197. [CrossRef]
19. Puso, M.A.; Solberg, J. A formulation and analysis of a stabilized nodally integrated tetrahedral. *Int. J. Numer. Methods Eng.* **2006**, *67*, 841–867. [CrossRef]
20. Al-Milli, S.; Seneviratne, L.D.; Althoefer, K. Track-terrain modelling and traversability prediction for tracked vehicles on soft terrain. *J. Terramechanics* **2010**, *47*, 151–160. [CrossRef]
21. Liu, C.; Chen, W.H.; Andrews, J. Optimisation based control framework for autonomous vehicles: Algorithm and experiment. In Proceedings of the 2010 International Conference on Mechatronics and Automation (ICMA), Xi'an, China, 4–7 August 2010; pp. 1030–1035.
22. Wong, J.Y. *Theory of Ground Vehicles*; John Wiley & Sons: New York, NY, USA, 2008.
23. Dobrowolski LLC Company. Available online: https://www.dobrowolski.com.pl (accessed on 2 May 2023).
24. Air Force Institute of Technology. Available online: https://itwl.pl (accessed on 2 May 2023).
25. Silva, F.O.E.; Ferreira, L.H.D.C. Design and implementation of a PID control system for a coaxial two-wheeled mobile robot. In Proceedings of the IEEE International Symposium on Industrial Electronics, Taipei, Taiwan, 28–31 May 2013; pp. 1–6.
26. Khalaji, A.K.; Moosavian, S.A.A. Stabilization of a tractor-trailer wheeled robot. *J. Mech. Sci. Technol.* **2016**, *30*, 421–428. [CrossRef]